

Low-level image processing for early faint asteroid detection in the Hera mission

M. Eng. Dominik Markowski ⁽¹⁾, M. Eng. Enrico Melone ⁽²⁾, M. Sc. Steeve Kowaltschek ⁽³⁾

⁽¹⁾ AOCS & GNC Sensors Engineer, TEC-SAS, HE Space for European Space Agency,
dominik.markowski@ext.esa.int

⁽²⁾ AOCS & GNC Sensors Engineer, TEC-SAS, Aurora Technology BV for European Space Agency,
enrico.melone@ext.esa.int

⁽³⁾ Head of AOCS and GNC Sensors Unit, TEC-SAS, European Space Agency,
steeve.kowaltschek@esa.int

ABSTRACT

State-of-the-art image sensors and processing techniques are key enabling technologies for future planetary exploration missions. Hera is a European Space Agency mission aiming a binary asteroid system – Didymos and Dimorphos. The mission requires an image sensor and processing technique capable of detecting its target from a far distance. During the cruise, the main optical instrument – Asteroid Framing Camera (AFC) - will acquire several images with the faint target in the field of view. On ground, AFC images will be processed to detect the asteroid and to enhance prior knowledge of the asteroid ephemeris from ground astrometry. This paper presents an algorithm capable of enhancing the AFC camera performances and detecting faint targets with a magnitude of 8.3, where the limiting magnitude of state-of-the-art star trackers is between 5.5 and 6. High performance of the image processing is achieved through detailed analysis of AFC noise factors and its' dedicated filtering techniques. Noise identification is performed on AFC's detector, FaintStar, which had been artificially degraded to Hera end-of-life state. It includes a detailed analysis of fix-pattern noise (FPN), dark current non-uniformity (DCNU), random telegraph signal (RTS), saturated/dead pixels and baffle straylight background non-uniformity. The proposed image processing consists of FPN and DCNU compensation, RTS pixels identification and compensation, attitude estimation and stars removal. The performance of the algorithm is estimated based on artificially generated images and representative night-sky images acquired by the AFC engineering model.

1 Introduction

Hera is a planetary defense mission currently under development by the European Space Agency. It is scheduled for launch in October 2024 and rendezvous with the binary asteroid Didymos and its moon, Dimorphos, in December 2026. The primary objectives of Hera include a comprehensive analysis of the surface and interior properties of Didymos and Dimorphos, as well as a study of the outcome of NASA's Double Asteroid Redirection Test (DART). The DART spacecraft impacted Dimorphos in September 2022 to demonstrate the deflection technic of potential hazardous asteroid. The Hera spacecraft will rendezvous with the binary asteroid 2 years after impact. Its mission consists of a two-year cruise, which includes flyby of Mars and its' moon Deimos, followed by 18 weeks of characterization and observation of Didymos and Dimorphos from the initial 30km to as close as 4km at the end of the phase. This is followed by 6 weeks of autonomous proximity operations demonstration. [1]

During the cruise phase, at a distance of 10^6 km, a detection of Didymos with on-board Asteroid Framing Camera (AFC) must be performed to provide accurate pointing measurements needed for the last trajectory correction maneuver. Due to the expected low apparent magnitude of the target at the time of the detection (design target for detection 8.3) and the lack of active cooling of the AFC's detector, a dedicated image processing and noise compensation procedure is required. The approach is driven by a detailed characterization of AFC's performance and noise factors described in paragraph 2. The results of individual noise factors analysis and signal-noise-ratio analysis are used to select the optimal exposure time and provide further recommendations to be implemented in the detection procedure. The method, described in paragraph 3, consists of three sequences of frame acquisition with a recommended number of frames, frequency, delta pointing, and delays. It also involves a multi-step image processing pipeline deployed on the ground. The image processing pipeline utilizes several filters dedicated to major noise factors. This is followed by star-tracker-like pointing estimation and the detection of the asteroid on processed frames. The results are presented in paragraph 4, where the method is validated against synthetic images and the night sky demonstration performed by authors. Additionally, the robustness of the approach against worst day solar activity is demonstrated on synthetic images with proton-induced single event upset (SEU) pixels simulated on frames. Paragraph 5 concludes the paper with a critique of the results and highlights areas for further development.

2 AFC performance and noise analysis

The AFC is a mission-specific instrument built by JenaOptronik based on its existing product ASTROhead Cam. The configuration of the camera was developed to support its objectives in different mission phases: far range asteroid detection, science observations in spatial scales $3-0.01\frac{\text{m}}{\text{pixel}}$, and surface features detection for close range relative navigation. The camera is equipped with the CMOS APS sensor-on-a-chip FainStar developed by Caeleste. AFC achieves an angular resolution of 0.0054° per pixel, with 1022×1022 pixels detector and $5.5^\circ \times 5.5^\circ$ field of view optical system. [2] [3] The camera was characterized taking into consideration detector degradation due to radiation, straylight magnitude and environmental conditions expected during the detection of Didymos.

2.1 Baffle performance

The baffle used on the AFC is a direct re-use of the ASTRO-APS baffle designed for Sun Exclusion Angle $\text{SEA}=26^\circ$, however the application on the AFC is different as the Asteroid is needed to be detected when the angle is close to 60° . Baffle performance of the AFC flight model was tested by JenaOptronik on a test bench, which consists of azimuth and roll axis turntables and a solar sun simulator. The azimuth turntable allows to adjust angles between the AFC and Sun simulator to the expected Sun Exclusion Angle $\text{SEA}=60^\circ$. The roll axis turntable allows to verify baffle performance at different roll angles. As shown in Figure 1, baffle performance is excellent, resulting in very low level of straylight, that is uniform across the image. An average straylight signal measured over 80 frames with varying roll angle is $\overline{s_{sl}} = 303.20 \left[\frac{e^-}{s} \right]$ and its averaged standard deviation is $\sigma_{s_{sl}} = 33.77 \left[\frac{e^-}{s} \right]$. [4]

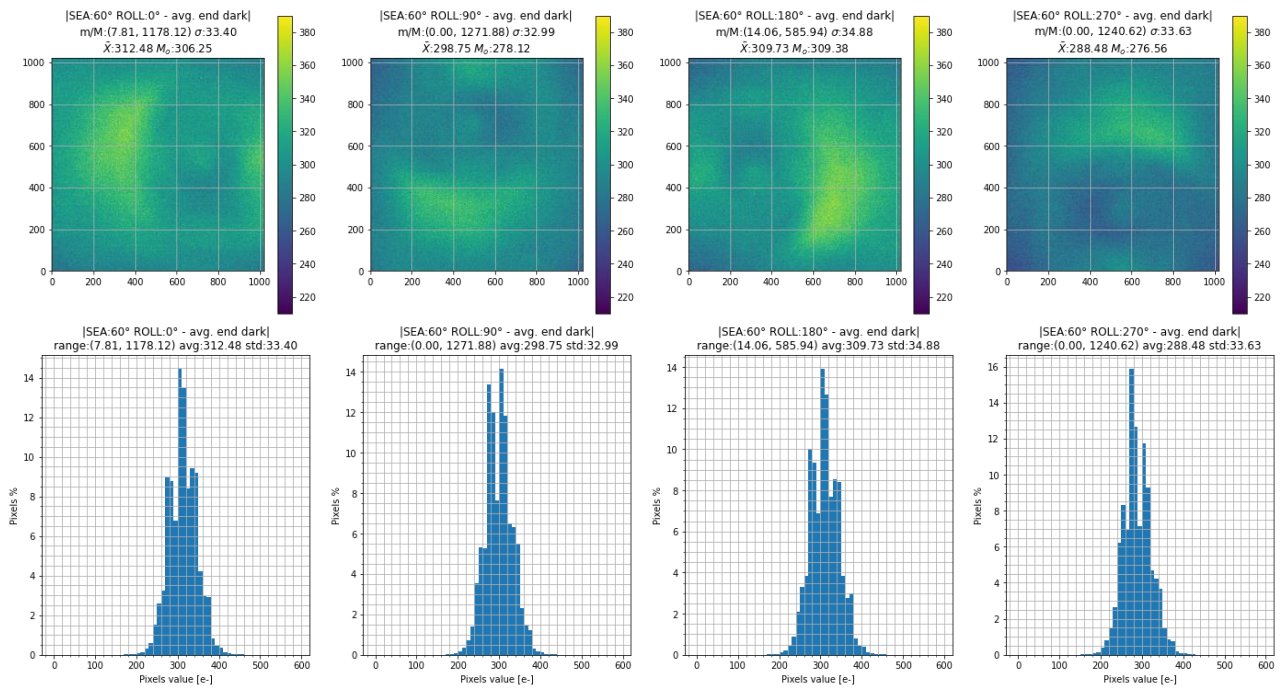


Figure 1 Straylight signal for SEA 60°

2.2 Optics performance

In the scope of the AFC FM Qualification and Acceptance Test [4], the Ensquared Energy (EE) values were measured before and after subjecting the system to vibration and TV-cycling, as well as analyzed within a temperature range of -2°C to 40°C. EE refers to the measurement of energy concentration within the area of a single pixel, considering a point light source centered on the pixel's center. EE measurements were conducted on 9 pixels located at the center, corners, and center of edges of the detector. No permanent degradation of EE was observed during vibration and TV-cycling. In the applicable temperature range of 19°C to 28°C, the EE value was found to be approximately 75%±0.5%. Based on the measured EE values, a Gaussian point spread function (PSF) was approximated and used to simulate the distribution of a single point source, such as a star-like signal, in the neighborhood of the signal projection. The maximal peak signal is achieved when the light source is centered on a pixel, while the worst-case scenario, resulting in a minimal peak signal, occurs when the light source is centered on an edge of 4 pixels, as shown in Figure 2 and Figure 3.

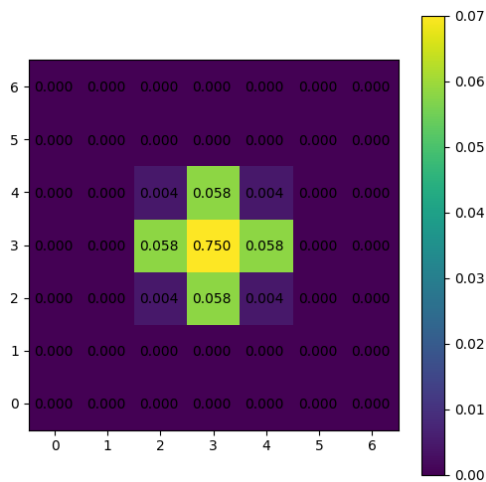


Figure 2 Signal distribution for a light source centered on a pixel.

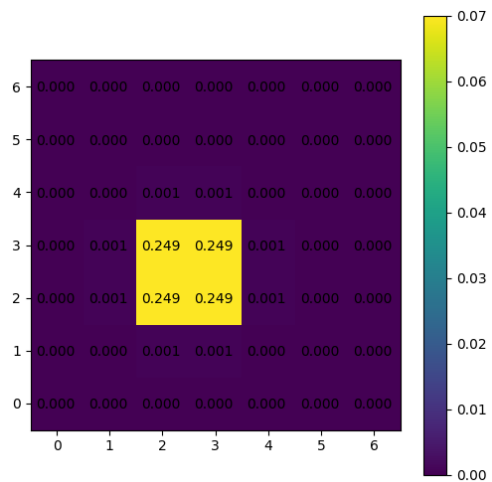


Figure 3 Signal distribution for a light source centered on an edge of 4 pixels.

2.3 Residual DCNU

Residual DCNU is an outcome of DCNU compensation and serves as a significant noise factor in detecting faint objects, as considered in this application. Residual DCNU was carefully characterised by a dark frames acquisition campaign performed on a Faint Star detector artificially irradiated to HERA's end-of-life level. The Device Under Test (DUT) had been placed in thermal chamber at temperatures: 0°C, 10°C, 20°C, 30°C, 40°C (detector temperature increased by 6°C due to self-heating) and sets of frames were acquired. The expected detector's temperature at the time of operation is estimated to be lower than 26°C. The acquisition cycle at each temperature setpoints consists of:

- 1 hour of temperature stabilization,
- acquisition of 10 frames $I_{fpnj=0\dots9}$ with $t_{exp} = 250\mu s$
- acquisition of 3611 frames $I_{dcnu_{k=0\dots3610}}$ with $t_{exp} = 1s$.

The produced data allows to calculate FPN noise and DCNU noise compensation based on 10 $I_{fpnj=0\dots9}$ frames and 10 $I_{dcnu_{k=0\dots9}}$ frames and to determine residual DCNU for any of $I_{dcnu_{k=10\dots3610}}$ frames, that were acquired $\Delta t_{dcnu} = 1s - 1h$ after the frames used for DCNU compensation. Firstly, $I_{dcnu_{k=0\dots3610}}$ frames were FPN compensated by subtracting the average of $I_{fpnj=0\dots9}$ frames. Secondary, $I_{dcnu_{k=0\dots3610}}$ frames were DCNU compensated by subtracting the average of first 10 $I_{dcnu_{k=0\dots9}}$ frames.

$$C_{fpn} = \frac{\sum_j I_{fpnj}}{10} \quad (Eq. 1)$$

$$C_{dcnu} = \frac{\sum_k I_{dcnu_k} - C_{fpn}}{10} \quad (Eq. 2)$$

Residual noise frames $R_{dcnu_{k=10\dots3610}}$ were calculated by compensation of frames $I_{dcnu_{k=10\dots3610}}$ with C_{fpn} and C_{dcnu} .

$$R_{dcnu_{k=10\dots3610}} = I_{dcnu_{k=10\dots3610}} - C_{fpn} - C_{dcnu} \quad (Eq. 3)$$

At detector's temperature equals 26°C, over 99.5% pixels of $I_{dcnu_{k=10\dots3610}}$ are well compensated, as shown in Figure 4. DCNU compensation is less effective with increased delta time Δt_{dcnu} between acquisition of $I_{dcnu_{k=0\dots9}}$ (used to calculate C_{dcnu}) and compensated frames – see green, orange and blue dashed lines in Figure 4. The remaining 0.5% of the pixels are affected by Random Telegraph Signal (RTS) effect. RTS noise is a random noise source characterized by unpredictable and rapid changes in signal magnitude between 2-4 discrete states. The noise can originate from charge trap in the oxide layer of the source follower in CMOS image sensors or metastability within the light collection area of detector. [5] Figure 5 displays the observed signal of a particle signal with the RTS effect. An increase of temperature amplifies RTS effect, both in terms of the number of affected pixels, as well as in terms of the frequency and delta value of RTS state changes, as depicted in Figure 6 and Figure 7.

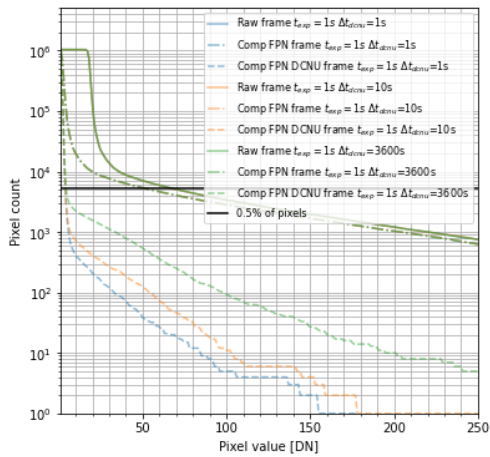


Figure 4 Cumulative distribution of raw frames, compensated frames at detector temperature 26°C.

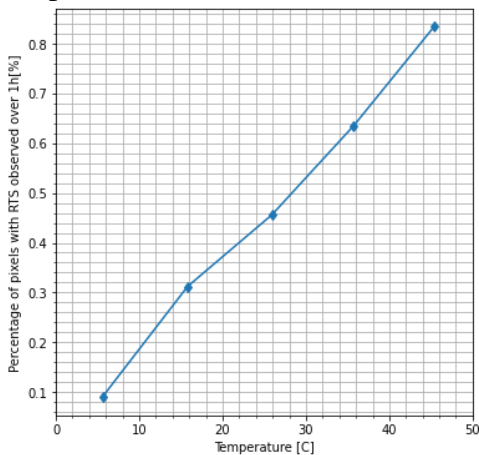


Figure 6 Percentage of pixels with RTS observed over 1h.

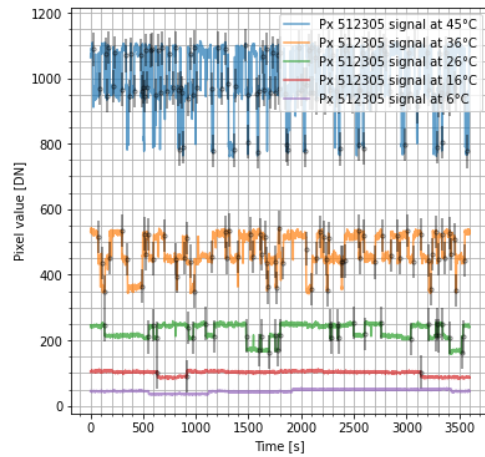


Figure 5 Pixel with RTS effect at different temperature.

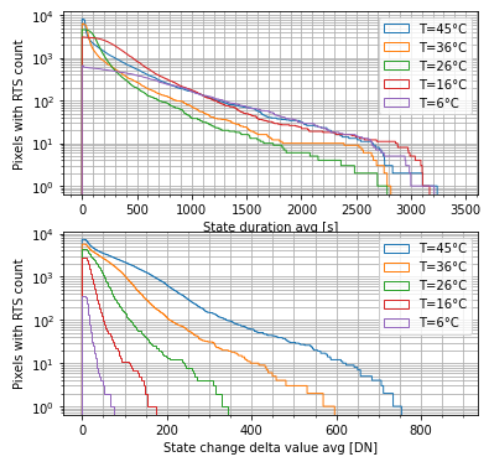


Figure 7 Cumulative histogram of RTS state change avg. duration and avg. delta value.

Residual DCNU level r_{dcnu} is defined as an upper threshold that encapsulate percentage of pixels without RTS. As shown in Figure 8, r_{dcnu} is increasing with higher detector's temperature and with delta time Δt_{dcnu} between acquisition of $I_{dcnu_{k=0..9}}$ (used to calculated C_{dcnu}) and compensated frames. Dark current signal is linearly proportional to exposure time t_{exp} , therefore residual DCNU level r_{dcnu} is also linearly proportional to exposure time.

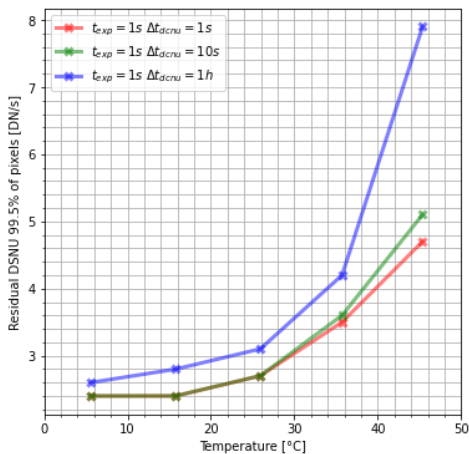


Figure 8 Residual DCNU - temperature dependence.

2.4 SNR analysis

Signal-noise-ratio (SNR) analysis has been performed to establish if target is detectable and to select the optimal integration time for the application. SNR is a dimensionless quantity calculated as a ratio of signal to square root of sum of noise factors' variances.

$$SNR = \frac{S_{sig} t_{exp}}{\sqrt{\sigma_{shot.sig}^2 + \sigma_{shot.dc}^2 + \sigma_{shot.sl}^2 + \sigma_{rn}^2 + r_{dcnu}^2 + \sigma_{prnu}^2 + \sigma_{quant}^2}} \quad (Eq. 4)$$

Target signal was estimated considering AFC model, which include optic aperture, signal PSF and crosstalk and average quantum efficiency times fill-factor across wavelength 370-1100nm. [4] [6] In worst case scenario, when signal from magnitude 8.3 source is centered at the corner of four pixels, 20% of total signal is registered $s_{sig} = 706 \left[\frac{e^-}{s} \right]$.

In scope of SNR analysis following noise sources are considered:

- signal shot noise, which standard deviation is equal: $\sigma_{shot.sig} = \sqrt{s_{sig} t_{exp}}$;
- straylight shot noise, which standard deviation is calculated based on baffle performance result presented in paragraph 2.1: $\sigma_{shot.sl} = \sqrt{\overline{s_{sl}} t_{exp}}$ where: $\overline{s_{sl}} = 303 \left[\frac{e^-}{s} \right]$;
- dark current shot noise, which standard deviation is calculated based on dark current reference value $D_{r.ref}$ and doubling temperature $T_{Dr.D}$ reported in [6]:

$$\sigma_{shot.dc} = \sqrt{t_{exp} D_{r.ref} 2^{\frac{T-T_{ref}}{T_{Dr.D}}}}$$
 ;
- residual DCNU r_{dcnu} , that is calculated based on the measurements described in paragraph 2.3 and as shown in Figure 8;
- photo response non-uniformity noise, which standard deviation is calculated based on PRNU factor ρ_{prnu} reported in [6]: $\sigma_{prnu} = \rho_{prnu} s_{sig} t_{exp}$ where: $\rho_{prnu} = 0.008$;
- quantization noise of ideal 12bit ADC is equal: $\sigma_{quant} = \sqrt{\frac{1}{12}} = 0.29 [DN] = 9.06 [e^-]$;
- read-out noise, which standard deviation is reported in [6]: $\sigma_{rn} = 25 [e^-]$.

The noise levels of individual noise sources against integration time and temperature are shown in Figure 9.

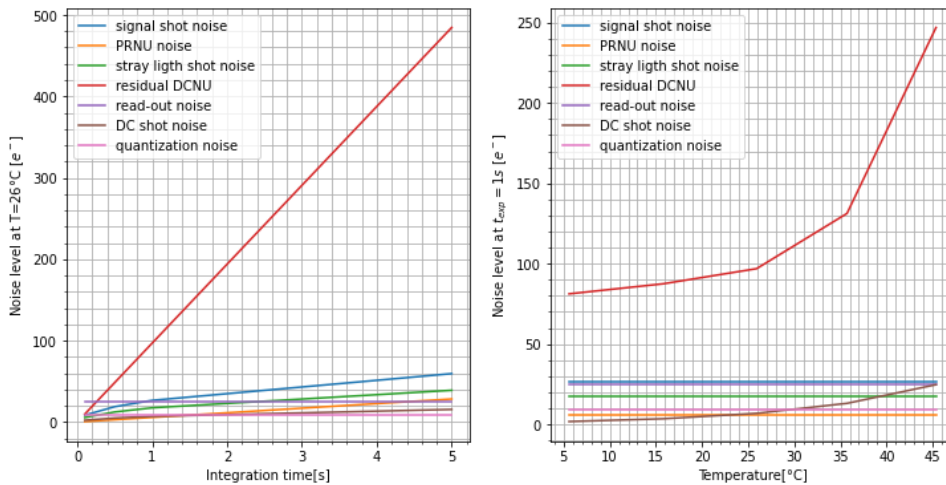


Figure 9 Integration time and temperature dependencies of individual noise sources.

SNR is increasing with integration time t_{exp} and its increase trend slows down after $t_{exp} = 1s$, as depicted in Figure 10. Longer exposure time t_{exp} causes lower acquisition frequency and longer DCNU compensation delta time Δt_{dcnu} , what result in amplification of RTS effect. Additionally, in case of solar flare, number of pixels affected by SEU is linearly proportional to t_{exp} . Therefore, it is concluded, that Didymos shall be detected on frame with $t_{exp} = 1s$. In case SEU producing environment and target's appearing magnitude lower than 8.3, t_{exp} can be reduced respectively to target's signal increase. SNR is higher with lower DCNU compensation age Δt_{dcnu} , therefore it is beneficial to detect the asteroid on frame acquired with minimal delay after DCNU compensation frames acquisition. Figure 11 illustrates SNR's temperature dependency. SNR is decreasing with temperature to the level where the detection of Didymos would be not possible or reliable at temperatures higher than 35°C.

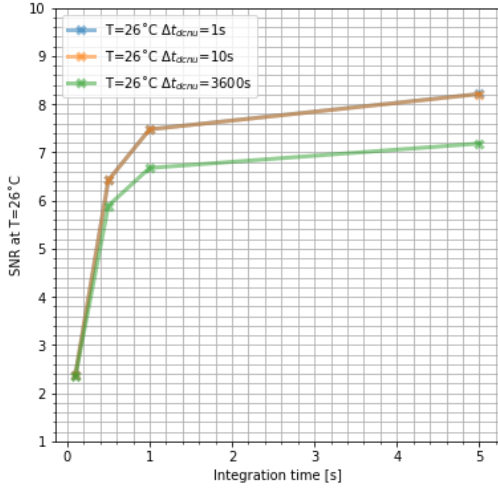


Figure 10 SNR at $T = 26^\circ\text{C}$ against integration time.

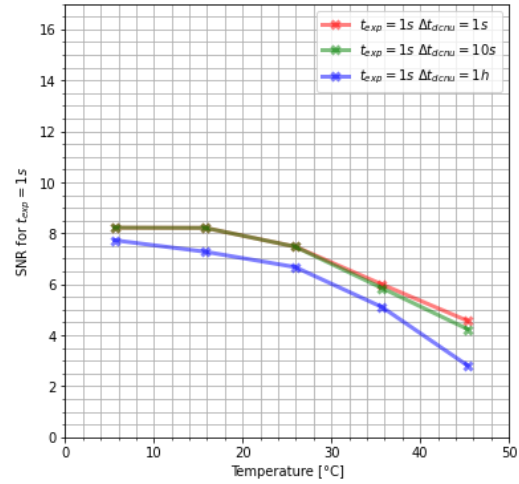


Figure 11 SNR for $t_{exp} = 1s$ against temperature.

3 Method

Based on results derived from SNR analysis and analysis of dark frames from irradiated detector to Hera end-of-life state, it was concluded that filtration of FPN, DCNU and RTS noise factor is needed to detect Didymos, which worst case appearing magnitude is 8.3. Additionally, to distinguish the asteroid from stars in FoV a solution based on star-tracker-like pointing estimation, followed by masking of stars based on its' reprojected position is included in the pipeline. In case of high solar activity during acquisition, dedicated SEU filter is added. From spacecraft operational point of view, the method can be separated into five steps:

1. Acquisition of 10 frames $I_{f_{pn}j=0\dots N_{f_{pn}}}$ with minimal detector's exposure time $t_{exp} = 250\mu s$.
The frames can be acquired pre-launch, but confirmation of FPN pattern during flight might be beneficial to verify no evolution of FPN and hot/dead pixels.
2. Acquisition of 11 frames $I_{dcnu_{k=0\dots N_{dcnu}}}$ with $t_{exp} = 1s$, that are used to calculate DCNU compensation. Delta pointing between two constitutive frames shall be $> 0.01^\circ$, to guarantee star-like objects' signal position change between frames. Didymos shall be in FoV. In scope of the paper, spacecraft angular velocity is assumed to be $0.05^\circ/s$ and frames $I_{dcnu_{k=0\dots N_{dcnu}}}$ are acquired with 0.5Hz frequency.
3. Acquisition of 3 or more frames $I_{t_{i=0\dots N_t}}$ with $t_{exp} = 1s$, that are used to detect Didymos after processing. Depending on target appearing magnitude and Solar flares activity it might be beneficial to reduce integration time, to minimize number of SEU pixel. Delta pointing

between two constitutive frames shall be significantly lower than AFC angular pixel resolution $\ll 0.0054^\circ$. Frames $I_{t_i=0\dots N_t}$ shall be acquired with minimal delay after step 2, needed to stabilized spacecraft pointing. In paper 1h delay between step 2 and 3 is assumed as sufficient.

4. Downlink of frames and on-ground image processing.

Figure 12 presents a high-level design of the faint object detection algorithm. Target frames $I_{t_i=0\dots N_t}$ are processed to reduce compensable noise factors like FPN, DCNU (including RTS) and SEU in case of high solar activity during acquisition. The computation of FPN and DCNU compensations utilizes respectively $I_{f_{pn}j=0\dots N_{f_{pn}}}$ and $I_{d_{cnu}k=0\dots N_{d_{cnu}}}$ frames. The filters are explained in paragraph 3.1. The star-tracker-like pointing estimation is described in paragraph 3.2. The asteroid identification on filtered frames is defined in paragraph 3.3.

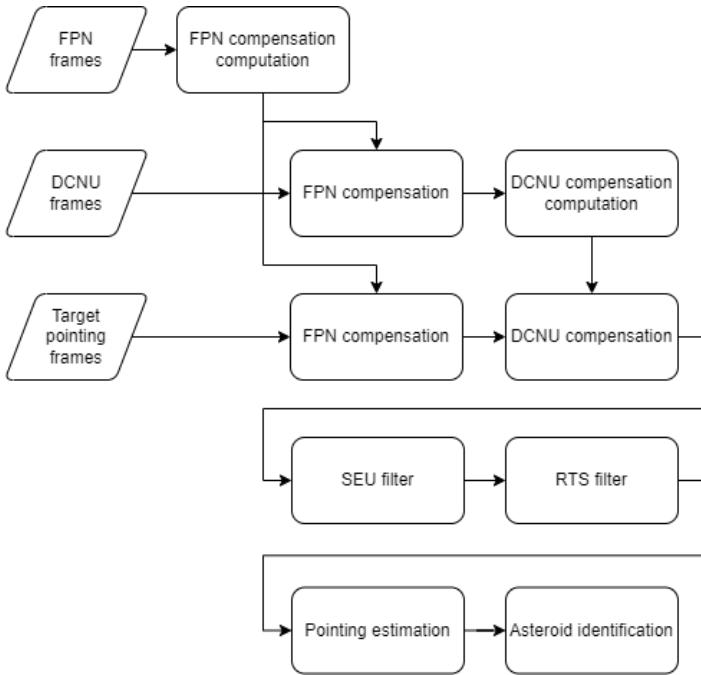


Figure 12 High-level overview of faint object detection algorithm.

3.1 Filters

3.1.1 Fix Pattern Noise compensation

Fix Pattern Noise, which is constant over time, radiation, and temperature, is mitigated with an offset matrix $C_{f_{pn}}$. The $C_{f_{pn}}$ matrix is calculated based on set of $N_{f_{pn}}$ short exposure time frames $I_{f_{pn}j=0\dots N_{f_{pn}}}$. The FPN noise present in the target frames $I_{t_i=0\dots N_t}$ is compensated with $C_{f_{pn}}$ subtraction. An example input and output of the FPN filter is visualized in Figure 13. On the left, a synthetic raw image with the target, stars, and SEU signal present in FoV is shown as the input. On the right side, the resulting image is depicted.

$$C_{f_{pn}}(x, y) = \frac{\sum_j^N I_{f_{pn}j}(x, y)}{N_{f_{pn}}} \quad (Eq. 15)$$

$$I_{t_i} := I_{t_i} - C_{f_{pn}} \quad (Eq. 16)$$

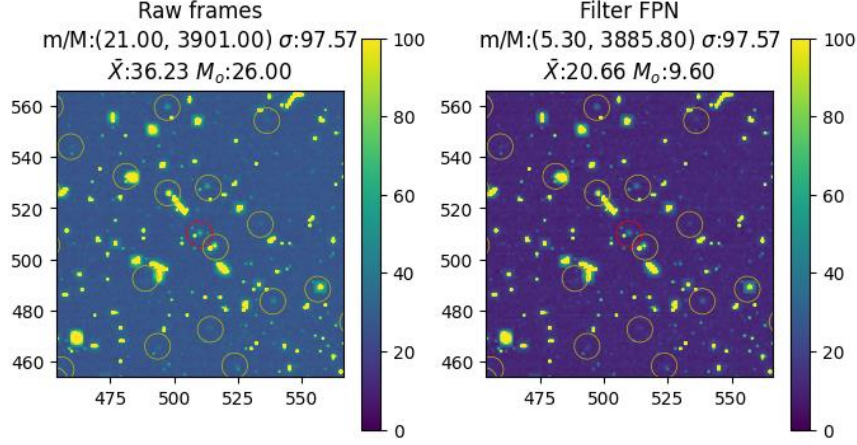


Figure 13 FPN filter input (left) and output (right). Asteroid marked with red circle, stars marked with gold circles.

3.1.2 DCNU compensation

Compensation of DCNU is traditionally achieved via deduction of average black image, but such method is not applicable for AFC due to absent of mechanical shutter and present of stars in the FoV. It is needed to segment which signal is introduced by star and which by noise to properly compensate DCNU. As the spacecraft is slightly rotating, signal from stars is travelling across pixel matrix, where DCNU signals are fix on specific pixels. One set of $I_{dcnu_{k=0\dots N_{dcnu}}}$ frames, outliers are detected using modified Niblack method on local 11x11 kernel [7]. Masks of outliers $O_{k=0\dots N_{dcnu}}$ are computed for $I_{dcnu_{k=0\dots N_{dcnu}}}$.

$$O_k(x, y) = \begin{cases} 1, & I_{dcnu_k}(x, y) > \mu_{bg.w_k}(x, y) + k_N * \sigma_{bg.w_k}(x, y) \\ 0, & I_{dcnu_k}(x, y) \leq \mu_{bg.w_k}(x, y) + k_N * \sigma_{bg.w_k}(x, y) \end{cases} \quad (Eq. 17)$$

where:

$$\mu_{bg.w_k} - \text{background wind. avg.}, \sigma_{bg.w_k} - \text{background wind. std.}, \\ k_N - \text{Niblack method parameter}$$

As windowed average and standard deviation is highly influenced by high signal SEU and star pixels present in the window, windowed background average and standard deviation ($\mu_{bg.w_k}, \sigma_{bg.w_k}$) are calculated based on I'_{dcnu_k} . I'_{dcnu_k} is calculated from I_{dcnu_k} , where pixels, with values higher than exclusion threshold $T_{bg.ex}$ above estimated background level - median of I_{dcnu_k} , are replaced with estimated background level. Threshold $T_{bg.ex}$ shall be significantly higher than 3 times std. of straylight.

$$I'_{dcnu_k}(x, y) = \begin{cases} I_{dcnu_k}(x, y), & I_{dcnu_k}(x, y) \leq Med(I_{dcnu_k}) + T_{bg.ex} \\ Med(I_{dcnu_k}), & I_{dcnu_k}(x, y) > Med(I_{dcnu_k}) + T_{bg.ex} \end{cases} \quad (Eq. 18)$$

where: $Med(I_{dcnu_k})$ - median of I_{dcnu_k} , $T_{bg.ex}$ - threshold \gg 3 std. of straylight

DCNU compensation matrix C_{dcnu} is calculated only for pixels classified as noise based on matrix V . To compute C_{dcnu} , a median value per pixel across $I_{dcnu_{k=0\dots N_{dcnu}}}$ frames is calculated and subtracted from an average background level per pixel, calculated as an average of μ_{bg_k} across N_{dcnu} frames.

$$V(x, y) = \sum_k^{N_{dcnu}} O_k(x, y)$$

$$C_{dcnu}(x, y) = \begin{cases} \frac{\sum_k^{N_{dcnu}} \mu_{bgk}(x, y)}{N_{dcnu}} - \text{Med}\left(I_{dcnu_{k=0\dots N_{dcnu}}}(x, y)\right), & V(x, y) > \frac{N}{2} \\ 0, & V(x, y) \leq \frac{N}{2} \end{cases} \quad (\text{Eq. 19})$$

DCNU noise present in target frames $I_{t_i=0\dots N_t}$ is mitigated by subtraction of the C_{dcnu} matrix. The performance of DCNU filter is shown in Figure 14.

$$I_{t_i} := I_{t_i} - C_{dcnu} \quad (\text{Eq. 20})$$

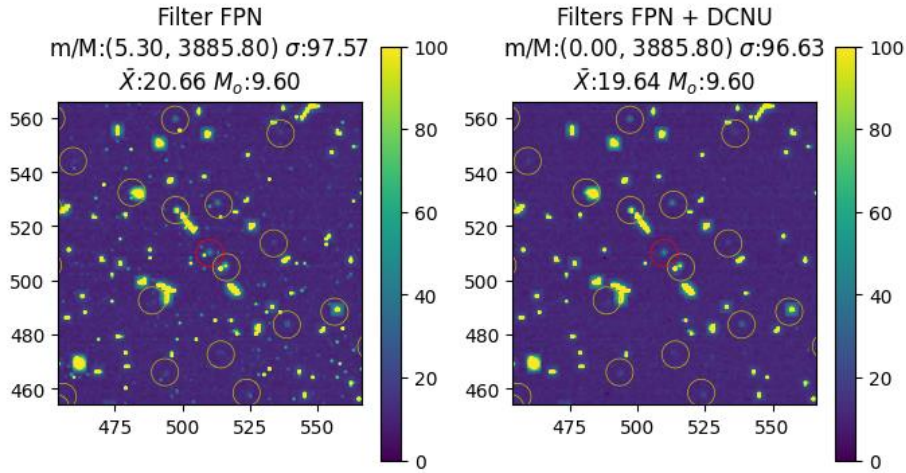


Figure 14 DCNU filter input (left) and output (right). Asteroid marked with red circle, stars marked with gold circles.

3.1.3 SEU filter

SEUs cause temporary high-value spikes or traces on the detector plane, which are reset during pixels readout. All $I_{t_i=0\dots N_t}$ frames are analysed pixel wise, to detect those temporary SEU pixels. Pixel (x, y) on frame I_{t_i} is classified as SEU, if its value is greater than minimal value of pixel (x, y) among the $I_{t_i=0\dots N_t}$ frames plus the threshold T_{seu} . The threshold T_{seu} shall be significantly higher than three times std. of the straylight.

$$I_{t_i}(x, y) = \begin{cases} I_{t_i}(x, y), & I_{t_i}(x, y) \leq \text{Min}(I_{t_i=0\dots N_t})(x, y) + T_{seu} \\ \text{Min}(I_{t_i=0\dots N_t})(x, y), & I_{t_i}(x, y) > \text{Min}(I_{t_i=0\dots N_t})(x, y) + T_{seu} \end{cases} \quad (\text{Eq. 21})$$

where:

$\text{Min}(I_{t_i=0\dots N_t})$ – pixelwise min of $I_{t_i=0\dots N_t}$,

T_{seu} – threshold $\gg 3$ std. of straylight

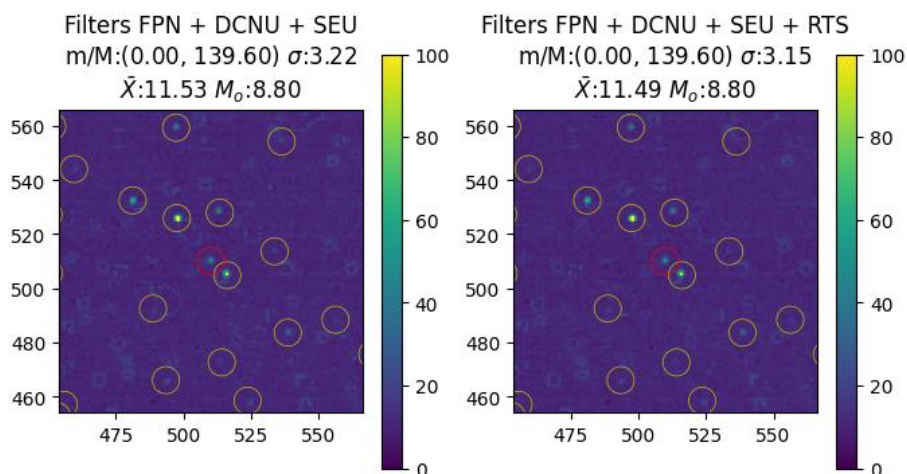


Figure 16 RTS filter input (left) and output (right). Asteroid marked with red circle, stars marked with gold circles.

3.2 Pointing estimation

Pointing estimation, which includes star extraction and centroid calculation, is performed using the Tetra3 library. This library is an example of a star tracker lost-in-space algorithm that was utilized within the scope of this paper. For the final implementation of the ground support software, the pointing estimation solution from existing ESOC libraries and knowledge will be reused. Further information on Tetra3 and its library can be found in references [8] and [9]. Star extraction from the target pointing frames $I_{t_i=0\dots N_t}$ is implemented in following steps.

1. Background subtraction.
Create the background image using a median filter with local 15x15 kernel and subtract pixelwise.
2. Image binarization
The threshold is calculated as a standard deviation of local 15x15 kernel scaled the factor 3.
3. Binary opening
Apply a binary opening operation with a 3x3 cross as structuring element to clean up the mask.
4. Create regions of image using binary mask.
5. Calculate centroids and statistics of regions.
6. Select set of regions for Tetra algorithm based on its' parameters like size, shape, and brightness.

Tetra algorithm solves the calibrationless lost-in-space problem in constant time and with a constant number of database accesses, in most cases exactly one. Tetra achieves its short runtime by performing any demanding work during the creation of its database of patterns. The patterns are stored as hashmap, what guaranties fast search. [8]

3.3 Asteroid identification

After filtering phases of the image processing pipeline, the frame exhibits a low background noise level, with FPN, DCNU, RTS, and SEU noises addressed. The significant signals remaining above the background level are associated with either stars or the asteroid. Based on the estimated AFC's pointing, the reprojected positions of stars in the field of view are calculated. Only stars brighter than magnitude 9.5 are considered, as fainter stars contribute negligible signals. For each star's position, its 7x7 neighborhood is analyzed. If an outlier (star) is detected in the neighborhood using the Niblack method, that star is removed from the image. The remaining outlier is associated with Didymos.

In the case of multiple remaining outliers, a ground operator shall manually analyze them across target pointing images $I_{t_i=0\dots N_t}$, taking into consideration the shape and brightness of the signals, and the prior knowledge of the asteroid's position, in order to identify the target. The autonomous detection layer is considered optional, as human operators are involved in the asteroid detection process on filtered images, this simple algorithm can complement their work.

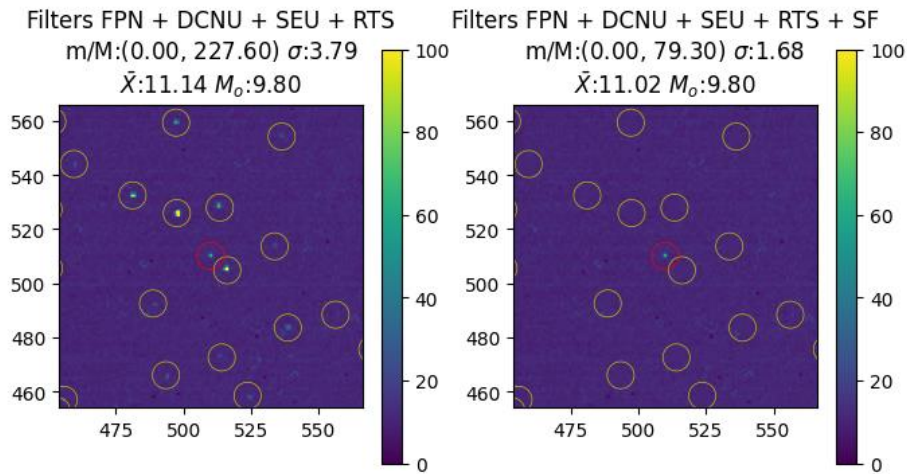


Figure 17 Star filter input (left) and output (right). Asteroid marked with red circles; stars marked with gold circles.

4 Results

The initial validation of the algorithm was conducted using synthetic images. These images were generated by adding stars and the target signal to dark frames captured with the FaintStar detector, which was irradiated to simulate the end-of-life state expected on the Hera mission. The number, frequency and timing of the $I_{f_{pn}j=0\dots N_{f_{pn}}}$, $I_{d_{cnu}k=0\dots N_{d_{cnu}}}$ and $I_{t_i=0\dots N_t}$ frames match the requirements listed in paragraph 0. The radiation environment prediction was calculated using the OMERE tool, as depicted in Figure 18. To generate the SEU signal, simulation of proton-induced SEU on the detector plane was performed using an ESA in-house tool [10], as shown in Figure 19. This SEU signal was then added to the synthetic images. As the detection can be performed over a few days, it was decided to show robustness to a Solar Flare corresponding to the worse-day (and not peak 5 minutes).

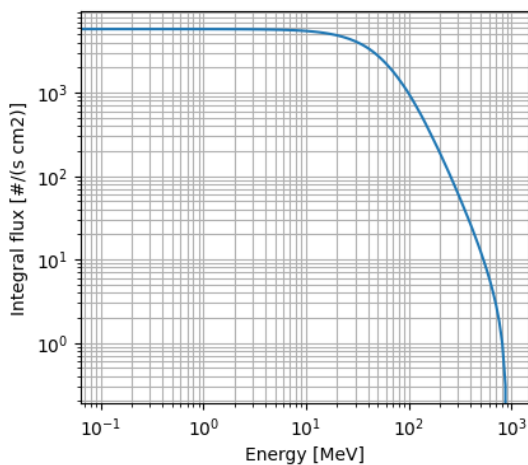


Figure 18 OMERE output - integral flux energy distribution.

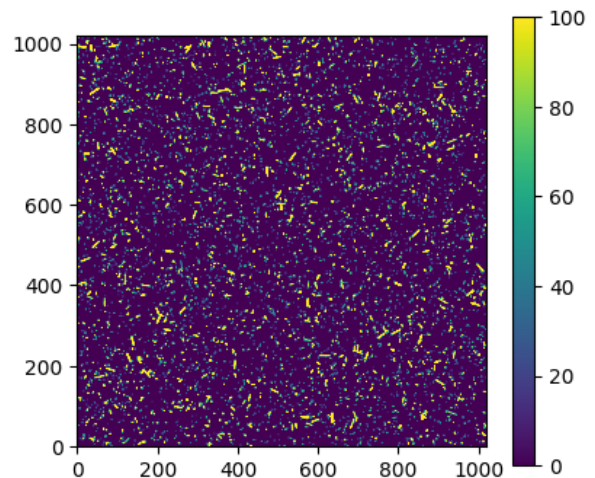


Figure 19 HERA AFC SEU signal simulation.

An example of synthetic image and its filtering process is illustrated in Figure 20. The method has successfully reduced total noise level to $\sigma_{TN} = 1.68DN$ and removed all stars and SEU pixels from the image leaving only the target's signal. In worst case scenario, when signal from magnitude 8.3 source is centered at the corner of 4 pixels, 20% of total signal is registered $s_T = 24DN$. This results in SNR equal $SNR = \frac{s_T}{\sigma_{TN}} = 14.29$.

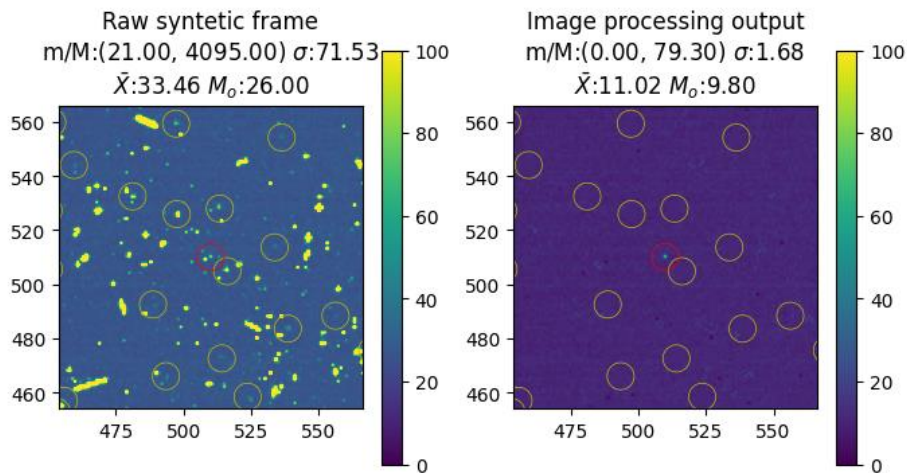


Figure 20 Image processing validation on synthetic image. Raw synthetic frame input (left) and output (right). Asteroid marked with red circles; stars marked with gold circles.

As part of a higher fidelity demonstration, a night sky test was conducted using a representative engineering model (EM) of the AFC, built internally at ESA. The EM was assembled with commercial off-the-shelf (COTS) optics that had similar parameters to the flight model (FM) and was paired with a baffle re-used from a previous contract with Jena Optroniks. The EM utilized a Faint Star detector that was proton-irradiated to simulate the end-of-life (EoL) state, providing representative noise levels present in the images. The details of the EM assembly and a comparison between EM and FM are listed in Table 1. The objective of the night sky test was to evaluate the image processing capabilities under representative conditions. Artificial light sources were used to generate straylight. The movement of the stars in the FoV was represented by the Earth's angular rotation.

The asteroid was simulated by selecting a star from the FoV with a similar appearing magnitude as the target. During the test, 10 frames with minimal detector's exposure time $t_{exp} = 250\mu s$ $I_{fpm\ j=0\dots N_{fpm}}$ were acquired. Followed by acquisition of 11 frames $I_{dcnu\ k=0\dots N_{dcnu}}$ with $t_{exp} = 1s$ and frequency 0.5Hz. Lastly, one frame I_t was taken with $t_{exp} = 1s$. Due to the Earth's continuous rotation, the requirement on pointing stability for I_t was not meet and as a result SEU filter could not be evaluated, as multiple constant pointing frames are required to remove SEU-induced noise. Figure 21 illustrates AFC EM on a rooftop during the night sky test.

The test provided a comprehensive evaluation of the image processing capabilities under representative conditions, considering hardware, straylight, star movement, and an asteroid-like target. The frame I_t and its filtering process are illustrated in Figure 22. The method has successfully reduced total noise level to $\sigma_{TN} = 1.21DN$ and removed all stars from the image leaving only the target's signal. The archived final SNR is equal $SNR = \frac{s_T}{\sigma_{TN}} = 19.83$.

	AFC FM	ESA AFC EM
Detector	Faint Star II	Faint Star II (EoL)
Optics	HERAR 106/3.9	TECHSPEC #85- 204
Focal length	106 mm	100 mm
Aperture	27 mm (f/3.9)	f/2.8 – f/22
FoV angle	5.5°x5.5°	5.8°x5.8°
Baffle	FM	EM (from JOP)

Table 1 AFC flight and engineering model comparison.



Figure 21 AFC EM – night sky test

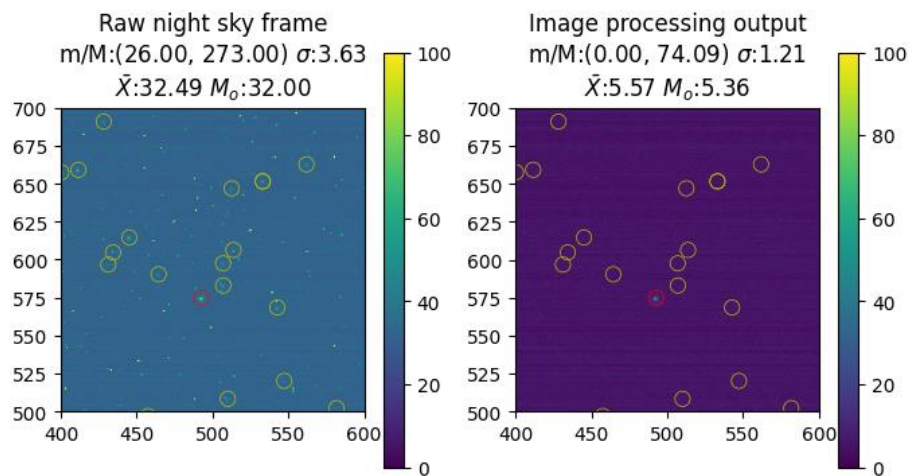


Figure 22 Image processing validation on night sky image. Raw night sky frame input (left) and output (right). Asteroid-like target marked with red circles, stars marked with gold circles.

5 Conclusion

In conclusion, this paper presents an algorithm that enables the detection of faint target, Didymos, with a magnitude of 8.3 with Hera on-board instrument AFC. The approach involves a comprehensive characterization of camera's performance and noise factors, leading to the selection of optimal exposure times and recommendations for the detection procedure. The image processing pipeline incorporates dedicated filters to mitigate major noise factors. Additionally, star-tracker-like pointing estimation and asteroid detection are implemented on the processed frames.

The effectiveness of the proposed method is proven, through validation using synthetic images and a night sky demonstration. The algorithm exhibits reliability and accuracy in detecting faint targets. Furthermore, the algorithm's robustness against SEU caused by worst-day solar activity is evaluated through simulations on frames.

In summary, this algorithm significantly enhances the capabilities of AFC, enabling the detection of faint targets beyond the capabilities of existing star trackers. Although, it is important to note that the proposed approach is design for on-ground processing and specifically tailored to the asteroid detection. Unlike state-of-the-art star trackers, this algorithm is not limited to on-board processing capabilities. This research establishes a foundation for advancements in planetary exploration

missions, particularly in the field of faint celestial-bodies detection by instruments embedding CMOS APS detectors.

Future development efforts should focus on further refining the algorithm while considering the specific limitations of the Hera spacecraft. These considerations include the downlink budget for the number of frames, on-board data handling and processing capabilities for acquisition frequency, and the spacecraft's pointing stability and agility required for necessary maneuvers. By addressing these aspects, the algorithm can be further optimized and its feasibility for application in Hera's mission context can be thoroughly evaluated.

Acknowledgments

The authors would like to express their sincere gratitude to all individuals and organizations who contributed to the successful completion of this research. The thanks are particularly addressed to Jena Optronik (Martin Zinner, Uwe Schmidt) and Caeleste (Werner Ogiers). Special thanks are extended to Emanuela Palombo for her invaluable scripts, as well as to Jesus Gil Fernandez and Hannah Goldberg from the Hera team for their seamless and pleasant cooperation. The authors also extend their appreciation to their colleagues at ESTEC and ESOC, whose advice, encouragement, and constructive criticism greatly contributed to this research.

Bibliography

- [1] P. Michel et al, "The ESA Hera Mission: Detailed Characterization of the DART Impact Outcome and of the Binary Asteroid (65803) Didymos," *The Planetary Science Journal*, vol. 3, no. 7, p. 160, July 2022.
- [2] Jena-Optronik, "ASTROhead Cam - Cameras & Camera Systems," [Online]. Available: <https://www.jena-optronik.de/products/cameras-and-camera-systems/astrohead-cam.html>. [Accessed May 2023].
- [3] Caeleste, "FaintStar - Caeleste," [Online]. Available: <https://caeleste.be/faintstar/>. [Accessed May 2023].
- [4] Jena Optronik, "HERA-JOP-AFC-RP-50020 - HERA AFC Test Summary," 2023.
- [5] B. W. Hendrickson, *Dark Current RTS-Noise in Silicon Image Sensors*, Portland, 2018.
- [6] ams Sensors Belgium, "FaintStar2 Datasheet: ICD and User Manual," 2021.
- [7] W. Niblack, *An introduction to digital image processing*, Englewood Cliffs: Prentice-Hall, 1986.
- [8] J. Brown and S. Keaton, "TETRA: Star Identification with Hash Tables," 2017.
- [9] European Space Agency, "tetra3," 2019. [Online]. Available: <https://tetra3.readthedocs.io>. [Accessed May 2023].
- [10] E. Palombo and S. Airey, "TN: A Simple Model For Proton Induced SEU Simulation," ESA, 2016.

